separations

MDPI

Article

Separation of Metal and Cathode Materials from Waste Lithium Iron Phosphate Battery by Electrostatic Process

Huabing Zhu [1], Yuxuan Bai [1,*], Lei Zu [1], Haijun Bi [2] and Jian Wen [1]

[1] School of Mechanical Engineering, Hefei University of Technology, Hefei 230009, China
[2] State Key Laboratory of Tea Plant Biology and Utilization, School of Tea and Food Science & Technology, Anhui Agricultural University, Hefei 230036, China
* Correspondence: fkpx99@163.com

Abstract: The improper disposal of retired lithium batteries will cause environmental pollution and a waste of resources. In this study, a waste lithium iron phosphate battery was used as a raw material, and cathode and metal materials in the battery were separated and recovered by mechanical crushing and electrostatic separation technology. The effects on material electrostatic separation of separation parameters such as the crushing particle size, the voltage of the static electrode, and the rotating speed of the grounding rotor were all studied combined with trajectory simulation and separation experiments. The results show that the crushing particle size of the material has the most significant impact on the separation effect, and the material separation effect primarily occurs in the range of 0.2–2.0 mm particle sizes. When the voltage of the static electrode is 30 kV, the rotating speed of the grounded rotor is 60 r/min, and the particle size is 0.4–0.8 mm, and the recovery rates for aluminum, copper, and lithium iron phosphate reach 93.2%, 91.1%, and 97.1%, respectively. In the recovery process for waste lithium batteries, using electrostatic separation technology instead of high-temperature roasting or chemical leaching can effectively improve the separation efficiency and reduce secondary pollution.

Keywords: electrostatic sorting; spent lithium iron phosphate battery; particle size range; cathode material recovery

check for updates

Citation: Zhu, H.; Bai, Y.; Zu, L.; Bi, H.; Wen, J. Separation of Metal and Cathode Materials from Waste Lithium Iron Phosphate Battery by Electrostatic Process. *Separations* **2023**, *10*, 220. https://doi.org/10.3390/separations10030220

Academic Editors: Sherif A. Younis and Mohamed Betiha

Received: 5 February 2023
Revised: 13 March 2023
Accepted: 20 March 2023
Published: 22 March 2023

Copyright: © 2023 by the authors. Licensee MDPI, Basel, Switzerland. This article is an open access article distributed under the terms and conditions of the Creative Commons Attribution (CC BY) license (https://creativecommons.org/licenses/by/4.0/).

1. Introduction

Lithium iron phosphate batteries have been widely used in energy storage equipment, electric vehicles, medical equipment, and other fields because of their high energy density, safety, cycle life, and good economic value. The scrap amount of such batteries will increase annually following their retirement period [1]. By the end of 2021, China's total scrap of new energy power batteries has reached 27 GWh, and it is expected to reach 74.2 GWh by 2025 [2]. A large amount of solid waste is continuously generated in this process. However, without proper management and recovery measures, the metal elements in the battery, residual organic solvents, and volatile acid gases may pose serious threats to the environment [3]. On the contrary, the continuous expansion of the production scale of lithium iron phosphate batteries has led to a gradual increase in the demand for cathode materials. Therefore, the recovery of cathode materials and valuable metals from waste lithium iron phosphate batteries not only has broad economic potential, but also guarantees the sustainable development of the battery industry, thereby reducing pollution emissions and resource waste. Considering that the composition of the lithium battery is complex and diverse, and the material regeneration process chain needs high-purity materials, the environmentally friendly and efficient material separation technology is a necessary process in the material recovery process.

Typical recovery methods of waste lithium batteries primarily include pyrometallurgy, hydrometallurgy, biological metallurgy, and physical–mechanical recovery technology [4].

The pyrometallurgical route primarily uses high-temperature roasting or heat treatment technology to separate and recover valuable metals based on the thermal characteristics of solid waste. The high combustion temperature and high residence time in the roasting furnace can effectively destroy the organic content in the crushing products and achieve the thermal decomposition of cathode materials [5]. The traditional pyrometallurgy process has high recovery efficiency and a low recovery cost, but has high energy consumption [6]. Cathode materials easily decompose in large quantities under high-temperature roasting, and the metal elements therein are slagged in the process and are accompanied by a large amount of mass loss [7]. In addition, the organic components in the battery will be converted into harmful gases and discharged during this process, and the environmental affinity is low [8]. Meanwhile, hydrometallurgy uses chemical reagents to dissolve valuable metals in solution to achieve metal separation, enrichment, and extraction. This method has a strong effective separation ability, low energy consumption, relatively stable recovery products, and high purity [9,10]. However, during dissolution and extraction, the selective separation of metal ions is highly dependent on the equilibrium pH [11]. Therefore, the hydrometallurgy process needs to introduce acid, alkaline dissolution reagents, and extraction solvents, as well as produce certain secondary pollutants [12]. Such a recovery method lays particular emphasis on element extraction. The recovered electrode materials usually exist in the form of leachates, so a relatively complex follow-up treatment process is required to complete the recovery and regeneration of the materials to ensure the recycling performance of the recycled materials [13,14]. The bio-metallurgy route uses active microorganisms to recover the metal components in the crushing products of the battery, which has a high environmental affinity and a low cost [15]. However, it is not yet of industrial application value because of its long recovery cycle [15].

Physical–mechanical recovery technology processes waste batteries into crushing products of target particle sizes through mechanical disassembly and crushing, and then carries out separation and recovery through physical characteristic differences of various materials (such as density, permeability, resistivity, etc.) [16]. Such a recovery process generally does not add more chemical reagents, nor does it require the high-temperature treatment of materials. Cathode materials and various metal materials are effectively recovered in their original chemical form, which can effectively reduce the performance degradation in the multi-generation recycling of materials and shorten the material regeneration process chain [17,18]. In addition, lithium iron phosphate does not contain high-price rare metal components compared to lithium cobaltate, lithium manganate, lithium nickanate, or ternary materials batteries. Moreover, the traditional thermal and wet recovery schemes primarily focus on the selective recovery of high-value-added components, which leads to the low interest of relevant enterprises in the recovery of lithium iron phosphate batteries. Nevertheless, the mechanical recovery process does not aim to discard separation, which minimizes the loss of secondary materials in the recovery process and has a high economic affinity. In the previous study, we used eddy current separation technology to separate and recover the shear-crushing products of lithium iron phosphate battery and found that the separation efficiency under the laboratory scale could reach more than 90% when the particle size of the material reached about 20 mm [19]. However, it is very difficult to break a large number of metal foils into 20 mm regular flakes in industrial production, which are often accompanied by a large number of fine particles. The larger particle size will also make it difficult to control the shape of the crushed products, thereby bringing additional technical challenges to pretreatment and crushing. High-voltage electrostatic separation technology is a separation method that uses differences in the conductivity, dielectric constant, and density of material particles to separate the mixed material particles in turn. It has been widely used in the separation and recovery of minerals, waste circuit boards, and waste household appliances' broken parts [20]. High-voltage electrostatic technology has a significant effect on the separation of small-particle-sized mixed particles compared with eddy current separation [21]. Fangyang Yuan [22] achieved the separation of mixed particles by applying a static electric field in the classification area of the wet

classifier. They used silica particles in the range of 0.21–8.71 μm as raw materials for the classification and separation experiment, with a total separation efficiency of 61.9%. In terms of millimeter particle separation, Martins et al. [23] recovered aluminum and copper-clad steel in coaxial cables through electrostatic separation technology, with recovery rates of 94.53% and 99.68%, respectively. It is explained that even if the mixture is all conductive material, it can be electrostatically separated by the difference between conductivity and density under reasonable parameter conditions. Park et al. [24] proposed an electrostatic separation process to separate coating material and granular copper from the crushing products of waste cables. They pointed out that the electric field strength and the relative position of the separator are the main factors affecting recovery efficiency. Calin et al. [25] used electrostatic separation technology to separate and extract zinc and brass particles in alkali–zinc–carbon batteries. The metal recovery purity reached 92%, whereas the average recovery energy consumption per kilogram of mixed materials was only 0.048 kWh. However, lithium battery cathode materials often have strong conductivity, unlike other non-metallic materials, which makes them subject to electrostatic interference in high-voltage electrostatic separation, and which reduces the separation efficiency of cathode and metal materials [26]. Lithium iron phosphate material has excellent safety performance and cycle life; however, its resistivity is the highest among common cathode materials. Mg^{2+}, Mo^{6+}, and other components are often added in production to improve their conductivity; however, their resistivity remains much higher than other common cathode materials [27,28]. This is a defect in the performance of lithium iron phosphate, but it is conducive to its effective separation from metal materials in high-voltage electrostatic separation. However, further study is still needed for the optimal separation conditions and particle size application range.

This study discussed the possibility of separating and recovering cathode materials and metals from the crushing products of spent lithium iron phosphate batteries by high-voltage electrostatic separation technology, which was achieved by combining the numerical simulation and separation tests. The quantitative force and motion model of the conductor material in the separation process is established, and the effects of the voltage of the static electrode, the rotating speed of the grounding rotor, and the particle size of the crushing particles on the separation efficiency, among other factors, are discussed. In addition, the air resistance coefficient is introduced to modify the separation model and determine the best separation conditions. The model can directly guide the parameter adjustment in the separation process of lithium iron phosphate battery crushing products, providing technical feedback for particle size control in the pretreatment and crushing process as well as a theoretical reference for the separation and recovery of other types of battery crushing mixtures.

2. Materials and Methods

2.1. Materials

Lithium iron phosphate batteries contain complex components, primarily composed of a shell, cathode plate, anode plate, electrolyte, and diaphragm. The sample used in this study is the lithium iron phosphate power battery (model IFP20100140A-21.5) produced by Guoxuan Hi-Tech Power Energy Co., Ltd. (Hefei, China). The main component of the cathode conductive coating is lithium iron phosphate, which adheres to the aluminum foil under the action of the adhesive polyvinylidene fluoride (PVDF). The anode coating is composed of graphite and is adhered to the copper foil by water-soluble adhesive, while the electrolyte is primarily composed of lithium hexafluorophosphate ($LiPF_6$) or vinyl carbonate ($C_3H_4O_3$) and organic solvent. Meanwhile, the diaphragm is primarily a multilayer microporous membrane composed of polyethylene or polypropylene used to block the passage of electrons between the anode and cathode while allowing the free passage of lithium ions. Moreover, the battery shell is primarily divided into a steel shell, an aluminum alloy shell, and a plastic soft shell, which is used to protect the cell structure and carry electrolytes.

2.2. Discharge and Disassembly

Figure 1 shows the overall recovery process of lithium-iron phosphate batteries. After the decommissioned battery pack undergoes preliminary appearance inspection, capacity separation, and the grouping process, the battery monomer that can still be used will continue to serve in a lower-level working environment after reassembly. Lithium batteries with bulge, leakage, deformation, and other defects that fail to pass the performance test will be directly scrapped and enter the material recovery stage. The discarded battery is discharged in 5 wt% sodium phosphate solution for 5 h and then enters the five-axis machining center to punch and mill the end face. The cell, shell, and electrolyte can be separated efficiently through mechanical disassembly. After unwinding the inner core with the custom-made unwinding device, the cathode and anode plates will then fall off the plastic diaphragm and enter the fume hood for 3 h to remove the residual electrolyte.

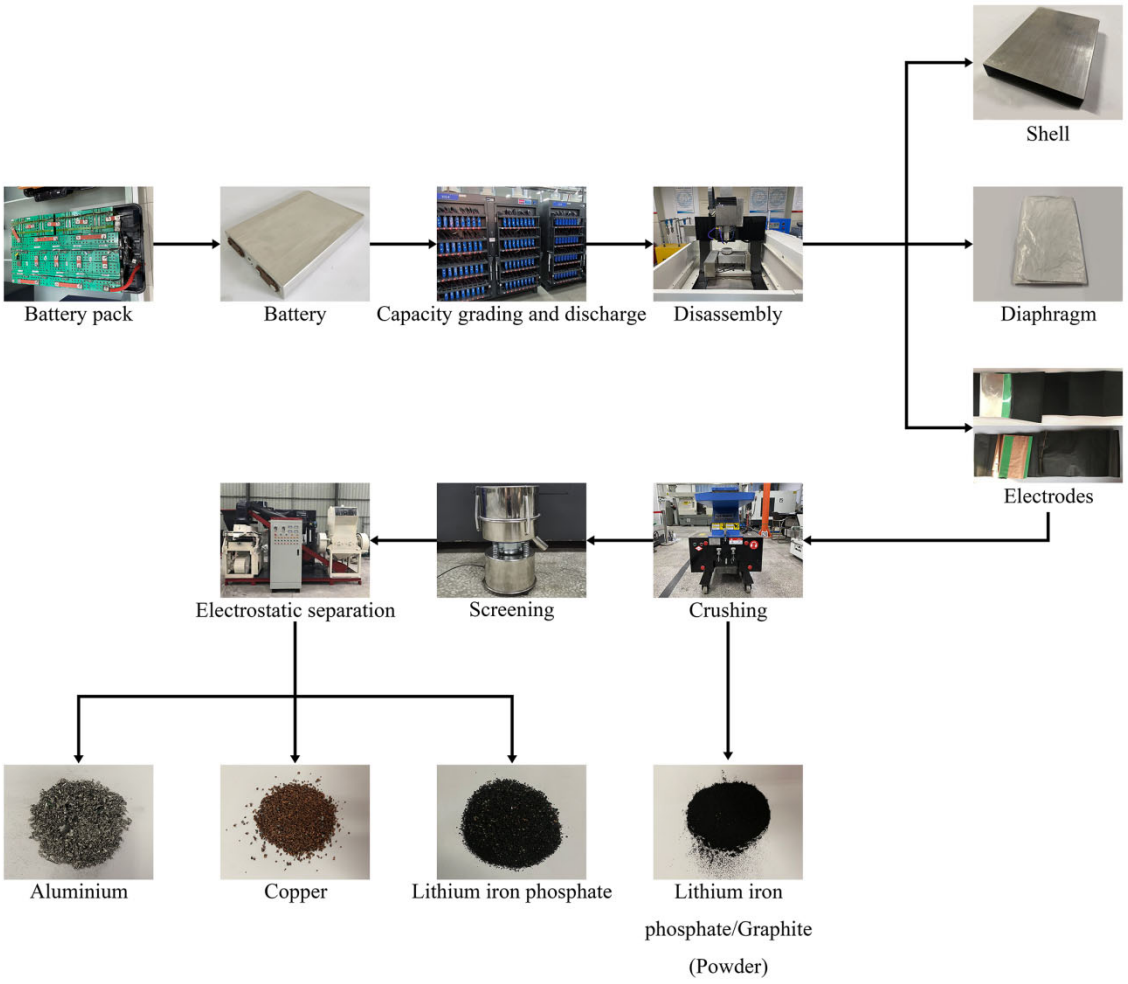


Figure 1. Recovery process of a waste lithium iron phosphate battery.

2.3. Pretreatment and Crushing

Given the existence of strong adhesive PVDF, aluminum foil and cathode coating are closely combined, but the traditional direct crushing method cannot completely peel the cathode coating from the metal surface while achieving particle size control [29]. Therefore, a proper pretreatment process is necessary. Considering that the PVDF melting point and thermal decomposition temperatures are 177 °C and 316 °C, respectively, this study conducts an orthogonal heat treatment test on the cathode plate under the condition of a treatment temperature of 200 °C–300 °C and a treatment time of 0.5–2 h, which is conducted in order to make PVDF lose its bonding effect to avoid toxic gas generation. The separation of cathode coating and aluminum foil is observed using a thermal field emission scanning

electron microscope to explore the best separation parameters. The equipment used in the experiment is Gemini 500 SEM, the detector type is SE2, the acceleration voltage is 3.00 kV, the working distance is 4.0–5.5 mm, and the magnification is 1000 times. After the low temperature heat treatment of the electrode, the electric core is treated with a rotary crusher for 20–80 s to obtain the comminuted products with different particle sizes. A seven-stage vibrating screen is used to screen the crushing products and count the particle size distribution. The mesh diameters produced are 4, 3.2, 1.6, 0.8, 0.4, 0.2, and 0.1 mm. After screening, according to the specific requirements of downstream enterprises, black substances with a particle size less than 0.2 mm or 0.1 mm will enter the downstream process chain and be purified through foam flotation. The remaining substances will enter the electrostatic separation stage after classified collection.

2.4. Establishment of High-Voltage Electrostatic Separation Model

A horizontal high-voltage electrostatic separator is used, and the separation device forms a corona charging area by combining the grounding rotor, the corona electrode, and the electrostatic electrode. Corona and static electrodes are used as the excitation source of the space electric field and connected with the negative pole of the high-voltage DC power supply, while the rotating rotor electrode is grounded. In addition, corona ionization occurs in the air medium around the corona electrode under a high-voltage direct current. The direction of the electric field affects the negative charge and flies to the rotating rotor electrode. Subsequently, the mixed material enters the charging area along with the grounded rotor and is charged after being bombarded by ions. Its movement is then separated into different tracks by the influence of electrostatic force and gravity effect, and the material separation is realized based on the difference in density and conductivity. The separation process and stress principle are shown in Figure 2.

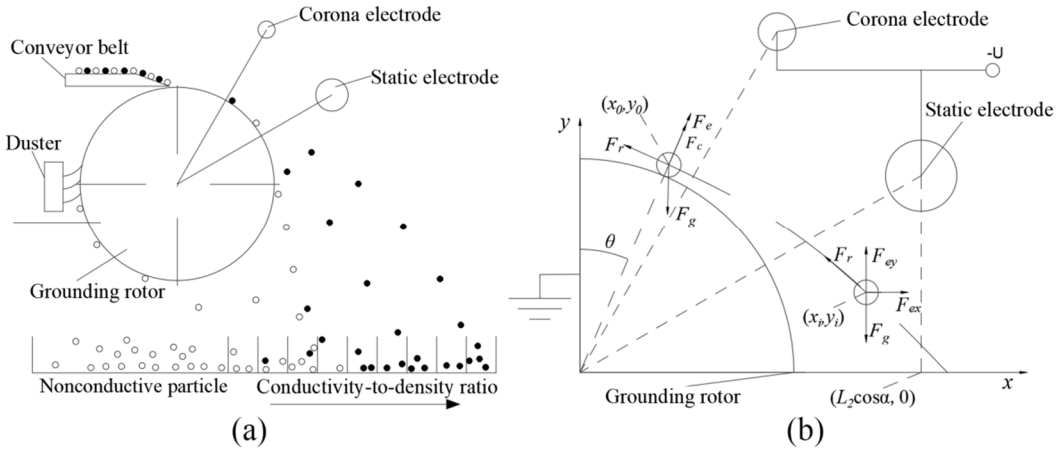


Figure 2. (**a**) Principle of electrostatic separation. (**b**) Force analysis of electrostatic separation.

COMSOL Multiphysics software is used to build the electric field intensity distribution model in the outer surface space of the grounding rotor and the space of the sorting cabin to quantify the effect of the electrostatic field on the acting force of conductor materials. A Fourier third-order fitting curve is used to quantify the simulation results, and the fitting expression is as follows:

$$E = a_0 + a_1 \times \cos(\theta \times w) + b_1 \times \sin(\theta \times w) + a_2 \times \cos(2 \times \theta \times w) + b_2 \times \sin(2 \times \theta \times w) + a_3 \times \cos(3 \times \theta \times w) + b_3 \times \sin(3 \times \theta \times w) \quad (1)$$

where a_0, a_1, a_2, a_3, b_1, b_2, b_3, and w represent the Fourier fitting function coefficients that are related to the fitting order and the input electric field strength data, and θ is the included angle between the measuring point roller center line and the vertical direction. When

conductor particles enter the corona ionization region, the particles will be corona-charged, and the change rule of their charge with the electric field strength is [30].

$$Q = \frac{2}{3}\pi^3 \varepsilon r_s^2 E \tag{2}$$

where ε and r_s represent the vacuum dielectric constant and the radius of the conductor material, respectively. The electrostatic force on the material can be expressed as follows:

$$F_e = QE \tag{3}$$

Based on the movement state, the movement mode of conductive materials in the high-voltage electrostatic separation process can be divided into two stages: the circular movement stage on the grounded rotor and the leap stage in the separation cabin. When the mixed material particles follow the grounding rotor into the ionization area ionized by the corona electrode, both the conductive and non-conductive material particles will enter the charging process. The electric field line density passing through its surface gradually increases as the motion proceeds. When the radial component of the applied force is not enough to provide the centripetal force, the material separates along the tangent direction of the arc under the action of the electric field force, thereby forming a leap motion, i.e., the (x_0, y_0) to (x_i, y_i) segments, as shown in Figure 2b. The critical relationship can be expressed as follows:

$$F_g \times \cos(\theta) = F_e + F_c \tag{4}$$

where F_e, F_c, and F_g are the electric field force of the material, the centrifugal force required to maintain the circular motion of the material, and the gravity of the material, respectively. The force balance condition can be formed of the following functions:

$$F_1 = \frac{4}{3}\rho\pi r_s^3 g \times \cos(\theta) - \frac{1.664}{3}\pi^3 \varepsilon r_s^2 E^2 \tag{5}$$

$$F_2 = \frac{16}{3}\rho\pi^3 r_s^3 n^2 R_1 \tag{6}$$

where F_1 and F_2 denote the component force of electric field force and gravity in the radial direction of the rotor and the centripetal force required by the material to maintain the circular motion, respectively. When the material rotates with the grounded rotor on the conveyor belt, the electrostatic force it receives gradually increases, and the radial component of gravity gradually decreases. When $F_1 \leq F_2$, the material separates from the rotor and leaps forward, solid particles with strong conductivity and low density, such as aluminum crushing products, are subjected to a large ratio of electrostatic force and gravity. Moreover, their separation position is relatively forward and the separation angle is small. Therefore, the component of their initial separation velocity in the horizontal direction is large, while the component in the vertical direction is small, their movement time in the leap movement process is longer, and the leap distance is far. This is one of the main characteristics of the effective separation of materials. Hence, the boundary conditions of particle movement in the separation chamber can be determined after the separation angle θ is solved by the critical equation above, where the initial coordinates are as follows:

$$\begin{cases} x_0 = R \times \sin\theta \\ y_0 = R \times \cos\theta \end{cases} \tag{7}$$

where R is the radius of the grounded rotor. The critical speed of particle separation is as follows:

$$\begin{cases} v_{x_0} = \frac{2\pi n}{60} \times R \times \cos\theta \\ v_{y_0} = \frac{2\pi n}{60} \times R \times \sin\theta \end{cases} \tag{8}$$

where n is the rotating speed of the grounding rotor. The horizontal and vertical force components of particles after separation are as follows:

$$\begin{cases} F_{x_0} = F_{e_x} - F_{f_x} \\ F_{y_0} = F_{e_y} + F_{f_y} - F_g \end{cases} \tag{9}$$

where F_e, F_r, and F_g denote the electric field force on the particle at the separation point, the air resistance on the particle, and the gravity on the particle, respectively. Therefore, the initial acceleration of particles after separation is as follows:

$$\begin{cases} a_{x_0} = \frac{[QE_x(x_0,y_0) - 0.5C_r\rho Sv]}{m} \\ a_{y_0} = \frac{[QE_y(x_0,y_0) + 0.5C_r\rho Sv]}{m} - g \end{cases} \tag{10}$$

However, it is difficult to calculate the real-time motion parameters of the conductor directly when the particles leave the grounded rotor and enter the leap motion phase because of the real-time change in the magnitude and the direction of electrostatic force they are subjected to. Furthermore, the field strength extraction in the simulation software is limited by the minimum grid. Therefore, the numerical solution of motion state based on iterative calculation can effectively obtain the particle motion trajectory. The iterative method is as follows:

$$\begin{cases} x_i = x_{i-1} + [v_{x_{i-1}}\Delta t_{i-1} + \frac{1}{2}a_{x_{i-1}}(\Delta t_{i-1})^2] \\ y_i = y_{i-1} - [v_{y_{i-1}}\Delta t_{i-1} - \frac{1}{2}a_{y_{i-1}}(\Delta t_{i-1})^2] \end{cases} \tag{11}$$

$$\begin{cases} v_{x_i} = v_{x_{i-1}} + a_{x_{i-1}}\Delta t_{i-1} \\ v_{y_i} = v_{y_{i-1}} - a_{y_{i-1}}\Delta t_{i-1} \end{cases} \tag{12}$$

$$\begin{cases} a_{x_i} = \frac{[QE_x(x_i,y_i) - 6\pi\eta r_s v_{x_i}]}{m} \\ a_{y_i} = \frac{[QE_y(x_i,y_i) + 6\pi\eta r_s v_{y_i}]}{m} - g \end{cases} \tag{13}$$

where x_i, y_i, v_{xi}, v_{yi}, a_{xi}, and a_{yi} denote the displacement, velocity, and acceleration of the conductor particles in the horizontal and vertical directions at the ith time point, respectively, and Δt is the time interval of iteration.

2.5. High Voltage Electrostatic Separation Test

The horizontal electrostatic separator is used for the separation test. The radii of the grounding rotor used and the electrostatic electrode are 114 mm and 19 mm, respectively; the arrangement angles of the corona and electrostatic electrodes are 60° and 30°, respectively; and the electrode spacing is 210 mm. After screening, the crushing products within each particle size distribution range will be subjected to an orthogonal test based on a 15–30 kV static electrode voltage and a 55–70 r/min grounded rotor speed. The test ambient temperature and the relative humidity of the air are 20 °C–25 °C and 35–45%, respectively. Multiple baffles in the aggregate device are installed, the falling area is gridded, the average leap distance is calculated based on the weight of the mass, and the sorting rate is counted under each group of optimal parameters. The calculation method of the average leap distance is as follows:

$$S = \sum \frac{m_i}{M} s_i \tag{14}$$

where S, m_i, M, and s_i represent the average leap distance, the collection mass of materials in each grid, the total material collection mass, and the horizontal distance from the grid to the center of the magnetic roller, respectively. The calculation method of the separation rate is as follows:

$$P = \sum \frac{m_i}{M} p_i \tag{15}$$

where P and p_i denote the recovery rate and the mass fraction of target material contained in each grid, respectively.

3. Results and Discussion

3.1. Pretreatment and Characterization

Figure 3 shows the scanning electron microscope characterization results of the cross-section of the cathode plate heat treatment test sample at different temperatures and treatment times. Despite the long-term use, the adhesive PVDF in the waste cathode plate still maintains good adhesion, and the thermal treatment temperature of 200 °C and below has a poor effect on the adhesion. After the cathode sheet is heat-treated at 250 °C for 2 h or at 300 °C for 30 min, the binder's effect is greatly weakened, and there is a gap between the cathode material and the metal surface, which will significantly affect the material stripping in the subsequent stage. Therefore, on this basis, further increasing the heat treatment temperature or heating time cannot continue to improve the dissociation effect. Considering that the above temperatures do not reach the critical conditions for the chemical decomposition of PVDF, the generation of toxic gases such as HF is avoided.

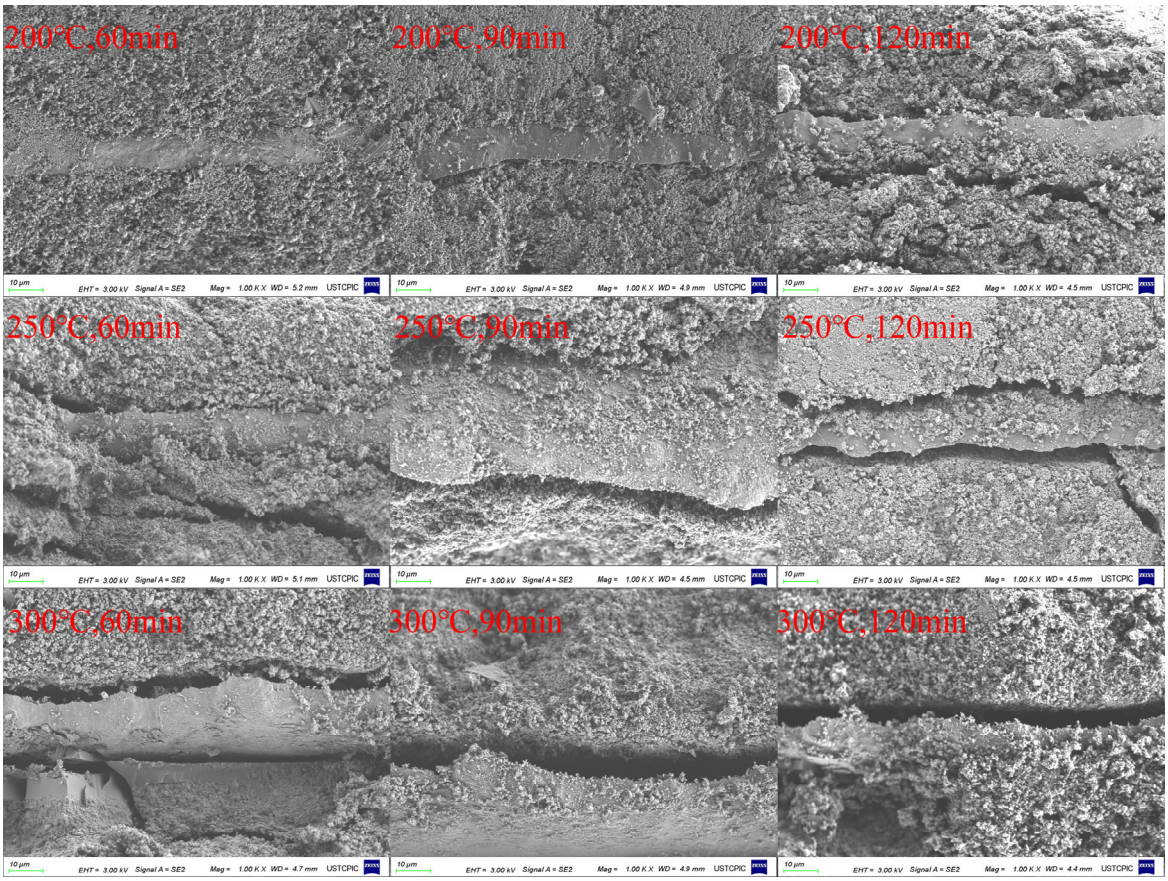


Figure 3. SEM images of cathode plate cross-section under different heat treatment conditions.

3.2. Crushing and Screening

Figure 4 shows the example of the crushing results of cathode and anode plates in the rotary crusher after the low-temperature heat treatment. The separation effect of the electrode material is good under the action of crushing stress because the heat treatment destroys the bonding effect between the coating and the metal foil. The screened copper and aluminum, lithium iron phosphate, and graphite are primarily distributed in the range of +0.4 mm, −0.8 mm, and −0.2 mm, respectively. Considering that the bonding effect of the water-soluble binder in the anode sheet is less than PVDF, the separation efficiency of copper foil and graphite in the anode sheet is higher than that of aluminum foil and lithium iron phosphate in the cathode sheet. The separation effect of the metal foil and electrode coating of small particle products is higher than that of large particle products because the

smaller particle radius often represents a more sufficient crushing effect. In addition, with the increases in crushing power and crushing time, the accumulation rate of each material in the small particle size range gradually increases. After the 80 s treatment of crushing products at 1500 w crushing power, all products enter the −0.4 mm particle size range; hence, the particle size distribution of crushing products is controllable and can be further adjusted based on the follow-up electrostatic separation feedback results.

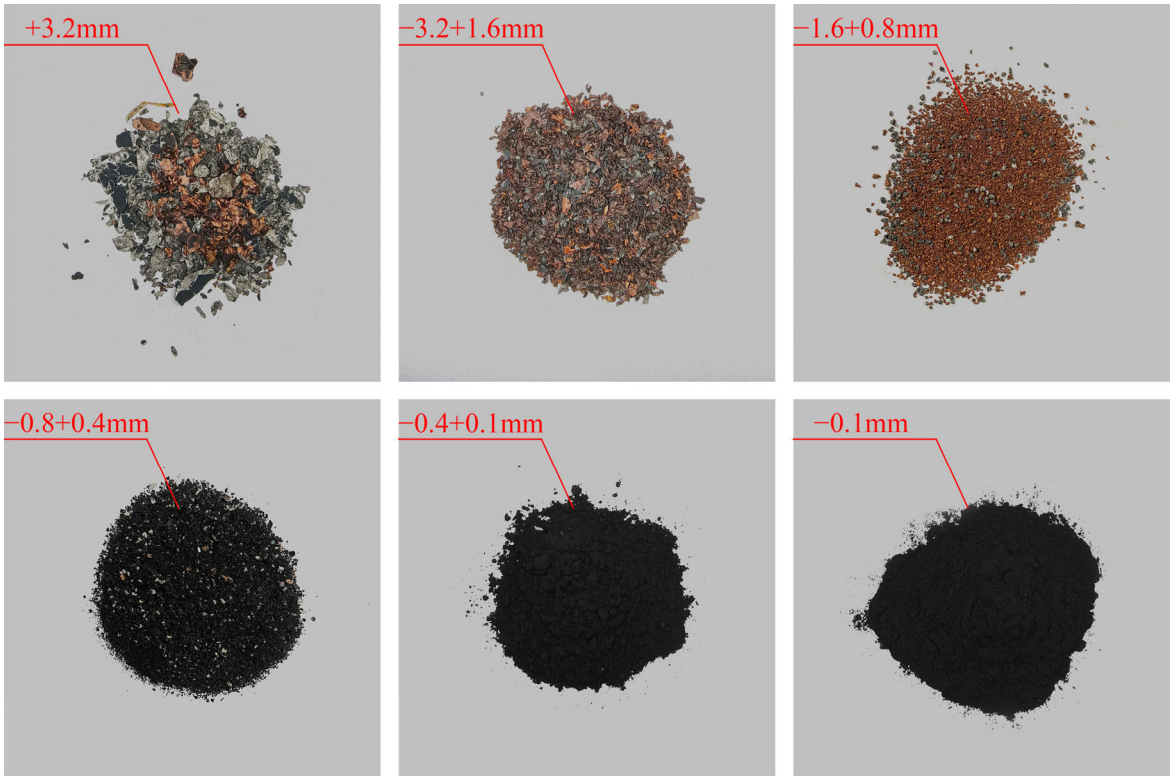


Figure 4. Distribution of each particle size of the crushed product of electric core.

3.3. Simulation and Analysis of High-Voltage Electrostatic Separation Process of Crushed Products

The COMSOL Multiphysics multi-field coupling software is used to construct the distribution of electric field intensity in the corona ionization region under different sorting parameters to dynamically extract the electric field intensity on the surface of the rotor. When the voltage of the static electrode is 20 kV, the size and direction distribution of the electric field intensity have an effect on the surface of the grounded rotor and in the separation space, as shown in Figure 5. Taking the rotation rotor axis as the Z axis direction, after the preliminary adjustment of the rotation rotor length in any plane perpendicular to the axis, the electric field line is parallel to the plane. As long as the length of the rotating rotor is far greater than the size of the material particles, the force of the material in different axial vertical planes will maintain the same change rule.

The electrostatic pole voltage changes to 15–30 kV, the electric field distribution of any plane perpendicular to the axis is intercepted for analysis, and the rule of the electric field intensity distribution is changed with the rotation angle of the grounding rotor, as shown in Figure 6. When the crushing products rotate with the grounded rotor, the electric field strength across the conductor surface increases initially and then decreases. Increasing the voltage of static electrodes can not only improve the overall electric field strength but can also make the peak of the electric field strength move forward, which is conducive to the early separation of the conductor material.

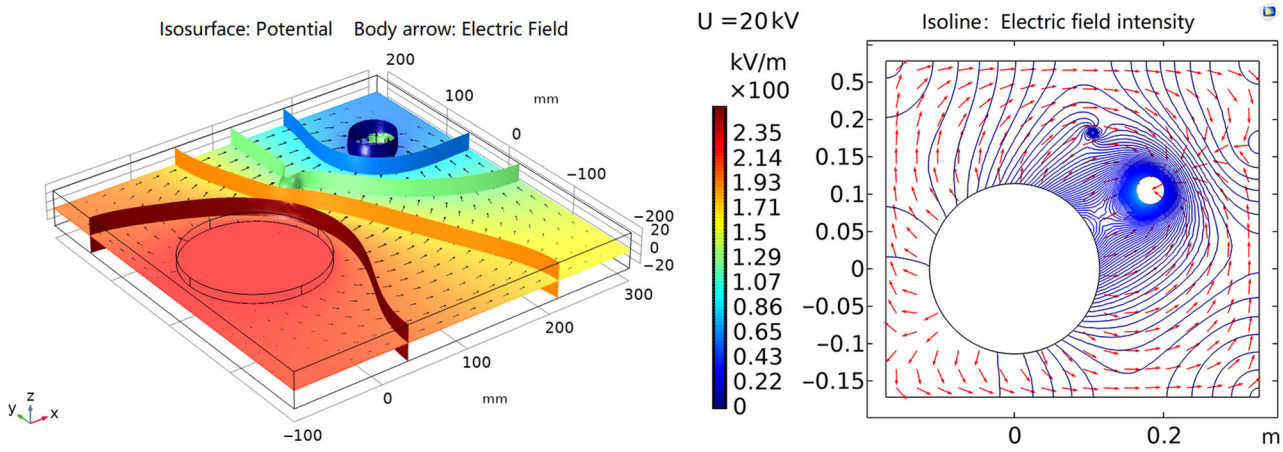


Figure 5. Simulation of electrostatic field distribution in the corona ionization region.

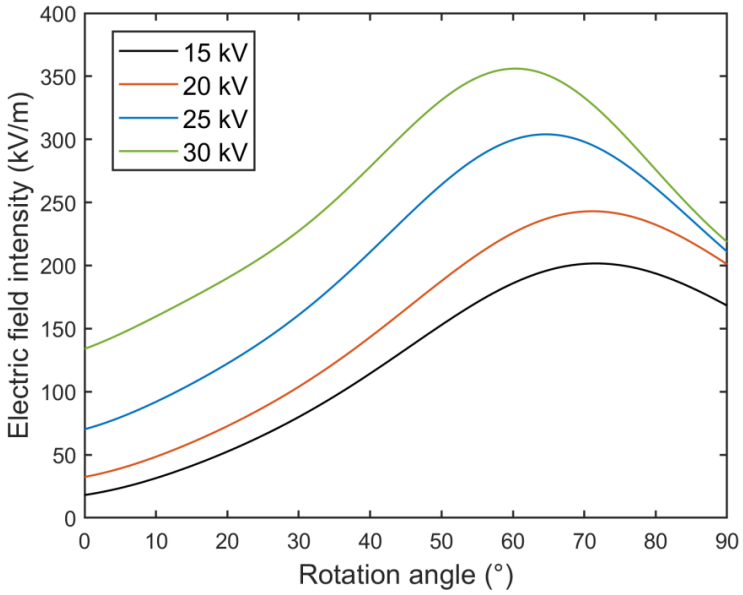


Figure 6. Variation of electric field intensity distribution with the rotation angle of the grounded rotor under different electrostatic pole voltages.

3.4. Fitting Results of Particle Motion Trajectory

The physical properties and electric field intensity distribution state of materials with different particle sizes are introduced into Formulas (5) and (6) to explore the initial position and critical motion state of material leap motion. Figure 7 shows the change in the stress condition state of the conductor material with the direction angle under the condition of each particle size. The intersection of the image shows the critical condition that the external force of the material only provides the centripetal force, i.e., the initial separation position of the material. Among them, the electrostatic forces of lithium iron phosphate particles with a particle size of 0.2–2 mm are all less than 10^{-5} μN. It is far lower than its gravity, and the calculated results of the critical detachment angle of each particle size are close to 90°; hence, it is difficult to synchronously mark them in the figure. This indicates that this material is hardly affected by electrostatic force, and its running track is approximately free-falling along the edge of the rotor, while the very small particles rotate with the rotor under the electrostatic adsorption and are finally removed by the dust collector. This is because the resistivity of lithium iron phosphate is more than 10^5 orders of magnitude different from that of copper, aluminum, and other metal materials, and has a very poor charging effect [31].

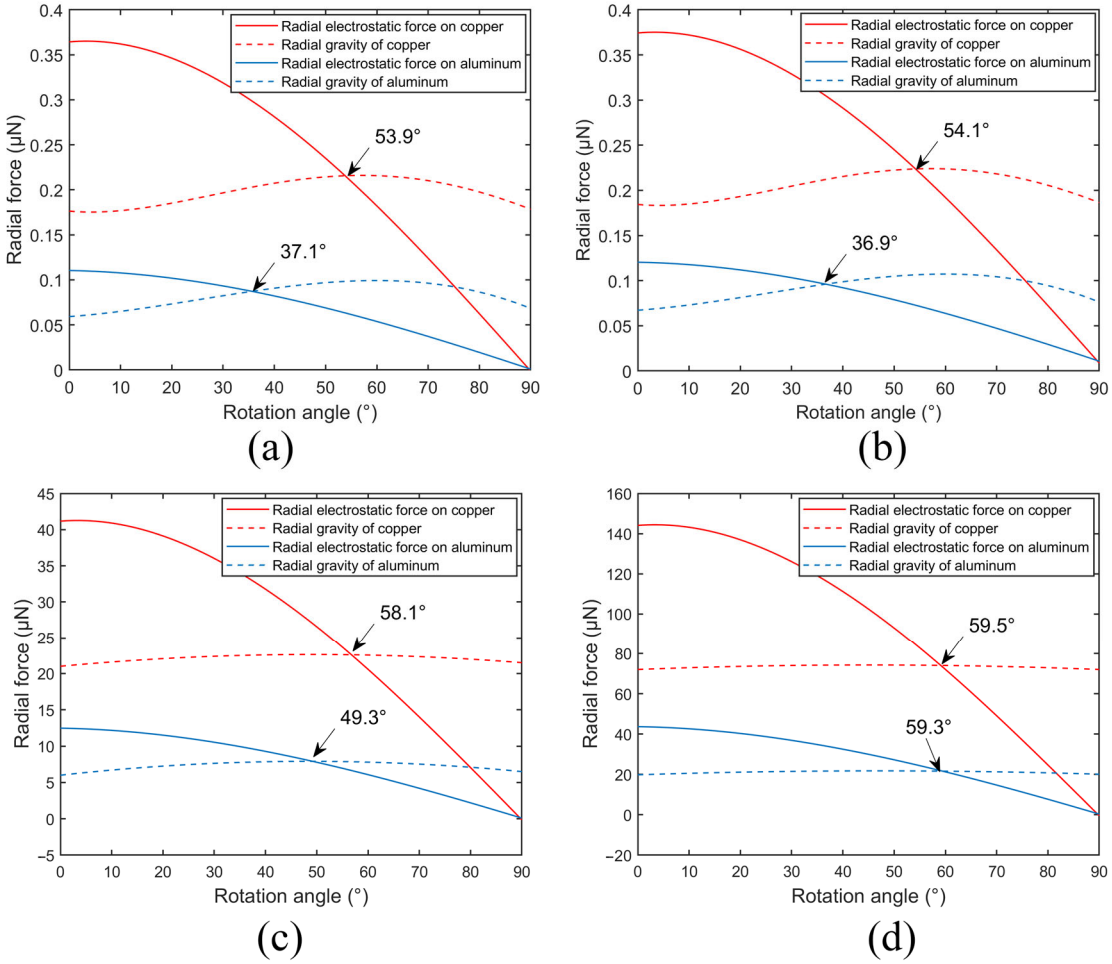


Figure 7. Calculation of detachment angle of metal particles with a particle size of (**a**) 0.2 mm, (**b**) 0.5 mm, (**c**) 1.0 mm, and (**d**) 2.0 mm.

By comparing the calculation results of the separation angle, it can be found that the separation angle of each component of the lithium battery crushing product is positively correlated with the particle size of the crushing product, and the mixture will leap in the order of aluminum > copper > lithium iron phosphate under the conditions of each particle size. For all particles, the separation order of different materials is primarily affected by the relative change amplitude of electrostatic force because there is a fixed proportional relationship between the component of gravity in the radial direction and the rotation angle. In addition, there is a small relative amplitude of the change in electrostatic force on large particles during material rotation with the rotor; hence, the separation angle difference between different conductive particles under the same particle size is small. Thus, forming a large leap time difference is difficult.

The calculation results of the above initial disengagement position and the initial force of the leap motion are substituted into the Formulas (7)–(13) based on the critical equation, and the running trajectory of each material is simulated in MATLAB. The iterative time step Δt is taken as 1×10^{-5} s, the falling height is 0.4 m, and the parameter adjustment range is the same as the departure angle simulation conditions. Based on calculation results, the horizontal displacement order of the material landing point is aluminum > copper > lithium iron phosphate, which is the same as the detachment order. Copper and aluminum fragments have the same motion characteristics; however, the motion state of copper is less affected by the electric field force because the density of copper is much higher than that of aluminum and the leap distance is short, while lithium iron phosphate is similar to free

fall. Taking the landing point distance between copper and aluminum as the separation distance, the simulation results under various conditions are shown in Figure 8.

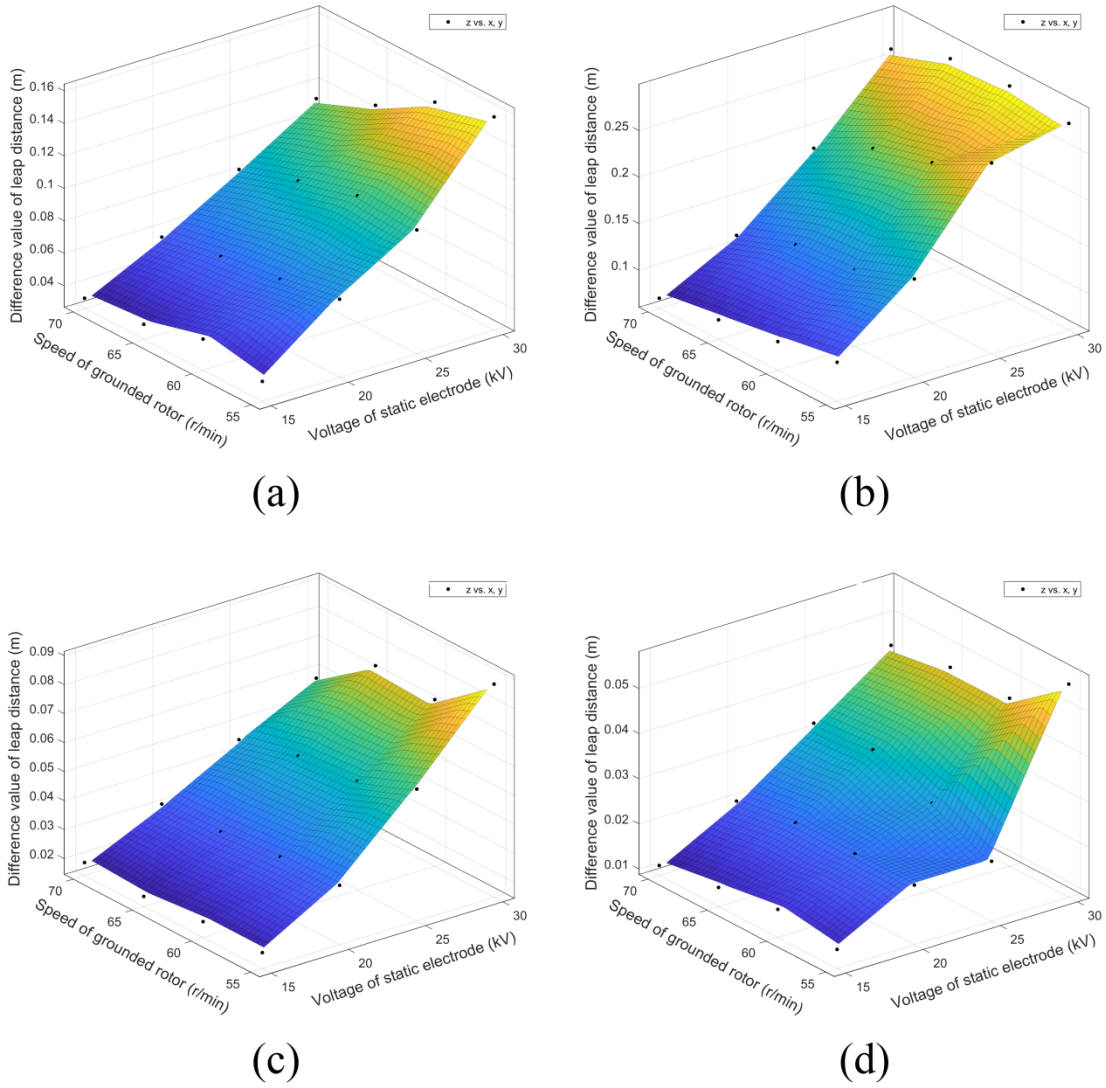


Figure 8. Effect of the voltage of static electrode and rotation speed of grounding roller on a separation distance of copper and aluminum under particle size of (**a**) 0.2 mm, (**b**) 0.5 mm, (**c**) 1.0 mm, and (**d**) 2.0 mm.

As shown in Figure 8, within the particle size range of 0.2–2 mm, the separation distance between different materials increases with the increase in electrostatic pole voltage, and initially increases and then decreases with the increase in material particle size and the rotation speed of the grounding roller. The key sequence of influencing factors is particle size > voltage of static electrode > rotation speed of grounding roller. Meanwhile, when the particle size is 0.5 mm, the electrostatic pole voltage is 30 kV, and the rotating speed of the roller is 55–60 r/min, the theoretical separation distance reaches the maximum. Furthermore, if the particle size range continues to be expanded, when the particle size of the crushing product is greater than 2 mm, the separation distance decreases monotonously and the value is less than 0.05 m. Therefore, crushing lithium iron phosphate battery products with a diameter of more than 2 mm are not suitable for electrostatic separation.

3.5. Analysis of Electrostatic Separation Test Results

The raw materials for the high-voltage electrostatic separation test are from the broken products of 80 lithium iron phosphate battery cells. In the experiment, the coating material

fell freely along the edge of the rotor, and there was almost no overlap area with the metal material. Hence, the separation effect is good. Therefore, the separation distance of copper and aluminum particles and the separation rate of aluminum weighted by mass were used as the separation effect indicators in the test. The experimental results are shown in Tables 1–4. Basically, with the increase in the electrostatic pole voltage, the separation distance and separation rate of all materials increase simultaneously. With the increase in particle size and the rotating speed of the grounded rotor, the separation distance and separation rate initially increase and then decrease. The particle size of the mixed material is the most significant factor affecting the separation effect, which is consistent with the simulation results. The average leap distance of all materials is close to the theoretical prediction results and is positively correlated with the material separation rate, which indicates that the theoretical separation distance can be used as an indicator of the expected separation effect of materials.

Table 1. Experimental results of electrostatic separation of aluminum and copper with a particle size of 0.2–0.4 mm.

Voltage of Static Electrode/kV	Difference Value of Leap Distance/m				Maximum Sorting Rate/%
	Speed of Rotor (55 r/min)	Speed of Rotor (60 r/min)	Speed of Rotor (65 r/min)	Speed of Rotor (70 r/min)	
15	0.041	0.046	0.036	0.032	77.9
20	0.072	0.07	0.061	0.056	77.5
25	0.101	0.103	0.088	0.081	82.4
30	0.150	0.148	0.117	0.102	84.9

Table 2. Experimental results of electrostatic separation of aluminum and copper with a particle size of 0.4–0.8 mm.

Voltage of Static Electrode/kV	Difference Value of Leap Distance/m				Maximum Sorting Rate/%
	Speed of Rotor (55 r/min)	Speed of Rotor (60 r/min)	Speed of Rotor (65 r/min)	Speed of Rotor (70 r/min)	
15	0.090	0.088	0.079	0.070	81.2
20	0.145	0.133	0.131	0.113	88.4
25	0.231	0.230	0.235	0.226	92.0
30	0.272	0.280	0.276	0.262	93.2

Table 3. Experimental results of electrostatic separation of aluminum and copper with a particle size of 0.8–1.6 mm.

Voltage of Static Electrode/kV	Difference Value of Leap Distance/m				Maximum Sorting Rate/%
	Speed of Rotor (55 r/min)	Speed of Rotor (60 r/min)	Speed of Rotor (65 r/min)	Speed of Rotor (70 r/min)	
15	0.020	0.020	0.018	0.019	73.9
20	0.034	0.035	0.032	0.031	73.5
25	0.058	0.052	0.049	0.043	77.4
30	0.078	0.072	0.063	0.055	81.9

Table 4. Experimental results of electrostatic separation of aluminum and copper with a particle size of 1.6–3.2 mm.

Voltage of Static Electrode/kV	Difference Value of Leap Distance/m				Maximum Sorting Rate/%
	Speed of Rotor (55 r/min)	Speed of Rotor (60 r/min)	Speed of Rotor (65 r/min)	Speed of Rotor (70 r/min)	
15	0.012	0.013	0.013	0.010	67.0
20	0.022	0.022	0.022	0.020	69.1
25	0.026	0.028	0.033	0.032	69.1
30	0.051	0.053	0.044	0.042	72.2

In addition, the experimental value of the average leap distance of each material is slightly lower than the simulation value, which may be because the selected particle size

has a certain distribution range, and some materials form irregular shapes during the crushing process. Hence, it is difficult to form the electrostatic force with a stable size and direction because the irregular shape often weakens the charging effect of the conductor in the corona charging area, and the stress characteristics are scattered in all directions, which weakens the leap effect and leads to the expansion of the landing point range, thereby increasing the size of the landing point overlap area between different materials [31,32].

When the voltage of static electrode is 30 kV, the rotating speed of the grounded rotor is 60 r/min, and the particle size is 0.4–0.8 mm, the separation reaches the optimal effect. At this time, the recovery rates of aluminum, copper, and lithium iron phosphate reach 93.2%, 91.1%, and 97.1%, respectively. Thus, based on this, the recovered products in the grid containing two kinds of mixed materials in the collector are subject to secondary electrostatic separation. The overall secondary recovery rates of the three materials above reach 95.4%, 92.1%, and 97.4%, and the tertiary recovery rates after a repeated separation process reach 95.7%, 92.4%, and 97.5%. When the number of electrostatic separation times increases, the separation ability is greatly weakened. From the collection results of the separated products, this phenomenon is primarily because the crushing products with extremely irregular shapes remain difficult to separate after multiple electrostatic separations. This indicates that when selecting the crushing method of waste lithium iron phosphate batteries, not only the particle size should be close to the optimal parameters but also the regularity and consistency of the shape of the broken products should be guaranteed as much as possible.

4. Conclusions

In this study, electrostatic separation technology was used to recover the metal and cathode materials from the crushing products of lithium iron phosphate batteries. The test results show that the low-temperature heat treatment technology reduces the difficulty of separating the cathode material and the current collector, and the material particle size is the most important factor affecting the electrostatic separation effect of the crushing products for the lithium iron phosphate battery. The electrostatic separation effect is mainly concentrated in the range of 0.2–2 mm material particle sizes. The material separation rate can be improved by increasing the voltage of the electrostatic electrode and properly reducing the rotating speed of the grounding rotor. The electrostatic separation method does not introduce additional chemical reagents and produces almost no polluting gas, which helps to improve the recovery rate and the purity of materials, and is highly environmentally friendly.

Author Contributions: Conceptualization, H.Z. and Y.B.; methodology, Y.B.; software, J.W.; validation, H.Z. and L.Z.; formal analysis, Y.B.; investigation, Y.B.; resources, H.B.; data curation, J.W.; writing—original draft preparation, Y.B.; writing—review and editing, H.Z.; visualization, H.B.; supervision, H.Z.; project administration, H.Z.; funding acquisition, H.B. All authors have read and agreed to the published version of the manuscript.

Funding: This research was funded by the National Natural Science Foundation of China [grant number 52205509] and by the Anhui Provincial Natural Science Foundation [grant number 2208085QE155], and by the Key Project of Natural Science Research in Anhui Universities [grant number KJ2021A0146], and Anhui Agricultural University Youth Fund [grant number k2135003] and The Open Fund of State Key Laboratory of Tea Plant Biology and Utilization, SKLTOF20220118).

Institutional Review Board Statement: Not applicable.

Informed Consent Statement: Not applicable.

Data Availability Statement: Data available on request due to restrictions, e.g., privacy or ethical. The data presented in this study are available on request from the corresponding author.

Conflicts of Interest: The authors declare no conflict of interest.

References

1. Kumar, J.; Neiber, R.R.; Park, J.; Soomro, R.A.; Greene, G.W.; Mazari, S.A.; Seo, H.Y.; Lee, J.H.; Shon, M.; Chang, D.W.; et al. Recent progress in sustainable recycling of $LiFePO_4$-type lithium-ion batteries: Strategies for highly selective lithium recovery. *Chem. Eng. J.* **2022**, *431*, 133993. [CrossRef]
2. Wang, Y.; Tang, B.; Shen, M.; Wu, Y.; Qu, S.; Hu, Y.; Feng, Y. Environmental impact assessment of second life and recycling for $LiFePO_4$ power batteries in China. *J. Environ. Manag.* **2022**, *314*, 115083. [CrossRef]
3. Makwarimba, C.P.; Tang, M.; Peng, Y.; Lu, S.; Zheng, L.; Zhao, Z.; Zhen, A.G. Assessment of recycling methods and processes for lithium-ion batteries. *Iscience* **2022**, *25*, 104321. [CrossRef] [PubMed]
4. Jin, S.; Mu, D.; Lu, Z.; Li, R.; Liu, Z.; Wang, Y.; Tian, S.; Dai, C. A comprehensive review on the recycling of spent lithium-ion batteries: Urgent status and technology advances. *J. Clean. Prod.* **2022**, *340*, 130535. [CrossRef]
5. Liu, W.; Zhong, X.; Han, J.; Qin, W.; Liu, T.; Zhao, C.; Chang, Z. Kinetic study and pyrolysis behaviors of spent $LiFePO_4$ batteries. *ACS Sustain. Chem. Eng.* **2018**, *7*, 1289–1299. [CrossRef]
6. Wang, M.; Liu, K.; Dutta, S.; Alessi, D.S.; Rinklebe, J.; Ok, Y.S.; Tsang, D.C. Recycling of lithium iron phosphate batteries: Status, technologies, challenges, and prospects. *Renew. Sustain. Energy Rev.* **2022**, *163*, 112515. [CrossRef]
7. Chen, M.; Ma, X.; Chen, B.; Arsenault, R.; Karlson, P.; Simon, N.; Wang, Y. Recycling end-of-life electric vehicle lithium-ion batteries. *Joule* **2019**, *3*, 2622–2646. [CrossRef]
8. Mao, J.; Li, J.; Xu, Z. Coupling reactions and collapsing model in the roasting process of recycling metals from $LiCoO_2$ batteries. *J. Clean. Prod.* **2018**, *205*, 923–929. [CrossRef]
9. Liang, Z.; Cai, C.; Peng, G.; Hu, J.; Hou, H.; Liu, B.; Liang, S.; Xiao, K.; Yuan, S.; Yang, J. Hydrometallurgical recovery of spent lithium ion batteries: Environmental strategies and sustainability evaluation. *ACS Sustain. Chem. Eng.* **2021**, *9*, 5750–5767. [CrossRef]
10. Jung, J.C.Y.; Sui, P.C.; Zhang, J. A review of recycling spent lithium-ion battery cathode materials using hydrometallurgical treatments. *J. Energy Storage* **2021**, *35*, 102217. [CrossRef]
11. Wang, F.; Sun, R.; Xu, J.; Chen, Z.; Kang, M. Recovery of cobalt from spent lithium ion batteries using sulphuric acid leaching followed by solid–liquid separation and solvent extraction. *RSC Adv.* **2016**, *6*, 85303–85311. [CrossRef]
12. Dang, H.; Li, N.; Chang, Z.; Wang, B.; Zhan, Y.; Wu, X.; Liu, W.; Ali, S.; Li, H.; Guo, J.; et al. Lithium leaching via calcium chloride roasting from simulated pyrometallurgical slag of spent lithium ion battery. *Sep. Purif. Technol.* **2020**, *233*, 116025. [CrossRef]
13. Chen, Z.; Zhang, L.; Xu, Z. Analysis of cobalt flows in mainland China: Exploring the potential opportunities for improving resource efficiency and supply security. *J. Clean. Prod.* **2020**, *275*, 122841. [CrossRef]
14. Liu, G.; Wang, N.; Qi, F.; Lu, X.; Liang, Y.; Sun, Z. Novel Ni–Ge–P anodes for lithium-ion batteries with enhanced reversibility and reduced redox potential. *Inorg. Chem. Front.* **2023**, *10*, 699–711. [CrossRef]
15. Roy, J.J.; Cao, B.; Madhavi, S. A review on the recycling of spent lithium-ion batteries (LIBs) by the bioleaching approach. *Chemosphere* **2021**, *282*, 130944. [CrossRef]
16. Thompson, D.L.; Hartley, J.M.; Lambert, S.M.; Shiref, M.; Harper, G.D.; Kendrick, E.; Anderson, P.; Ryder, K.S.; Gaines, L.; Abbott, A.P. The importance of design in lithium ion battery recycling–a critical review. *Green Chem.* **2020**, *22*, 7585–7603. [CrossRef]
17. Harper, G.; Sommerville, R.; Kendrick, E.; Driscoll, L.; Slater, P.; Stolkin, R.; Walton, A.; Christensen, P.; Heidrich, O.; Lambert, S.; et al. Recycling lithium-ion batteries from electric vehicles. *Nature* **2019**, *575*, 75–86. [CrossRef]
18. King, S.; Boxall, N.J. Lithium battery recycling in Australia: Defining the status and identifying opportunities for the development of a new industry. *J. Clean. Prod.* **2019**, *215*, 1279–1287. [CrossRef]
19. Bi, H.; Zhu, H.; Zu, L.; Bai, Y.; Gao, S.; Gao, Y. A new model of trajectory in eddy current separation for recovering spent lithium iron phosphate batteries. *Waste Manag.* **2019**, *100*, 1–9. [CrossRef]
20. Bedeković, G.; Trbović, R. Electrostatic separation of aluminium from residue of electric cables recycling process. *Waste Manag.* **2020**, *108*, 21–27. [CrossRef]
21. Rybarczyk, D.; Jędryczka, C.; Regulski, R.; Sędziak, D.; Netter, K.; Czarnecka-Komorowska, D.; Barczewski, M.; Barański, M. Assessment of the electrostatic separation effectiveness of plastic waste using a vision system. *Sensors* **2020**, *20*, 7201. [CrossRef] [PubMed]
22. Yuan, F.; Yu, J.; Zheng, X. Experimental study on fine particle separation in a wet electrostatic classifier. *Chem. Eng. Process. -Process Intensif.* **2020**, *156*, 108108. [CrossRef]
23. Martins, T.R.; Mrozinski, N.S.; Bertuol, D.A.; Tanabe, E.H. Recovery of copper and aluminium from coaxial cable wastes using comparative mechanical processes analysis. *Environ. Technol.* **2021**, *42*, 3205–3217. [CrossRef] [PubMed]
24. Park, C.H.; Subasinghe, N.; Jeon, H.S. Separation of covering plastics from particulate copper in cable wastes by induction electrostatic separation. *Mater. Trans.* **2015**, *56*, 1140–1143. [CrossRef]
25. Calin, L.; Catinean, A.; Bilici, M.; Samuila, A. A corona-electrostatic technology for zinc and brass recovery from the coarse fraction of the recycling process of spent alkaline and zinc–carbon batteries. *J. Clean. Prod.* **2021**, *278*, 123477. [CrossRef]
26. Xu, P.; Dai, Q.; Gao, H.; Liu, H.; Zhang, M.; Li, M.; Chen, Y.; An, K.; Meng, Y.S.; Liu, P.; et al. Efficient direct recycling of lithium-ion battery cathodes by targeted healing. *Joule* **2020**, *4*, 2609–2626. [CrossRef]
27. Li, J.; Ma, Z.F. Past and present of $LiFePO_4$: From fundamental research to industrial applications. *Chem* **2019**, *5*, 3–6. [CrossRef]

28. Wang, X.; Feng, Z.; Hou, X.; Liu, L.; He, M.; He, X.; Huang, J.; Wen, Z. Fluorine doped carbon coating of $LiFePO_4$ as a cathode material for lithium-ion batteries. *Chem. Eng. J.* **2020**, *379*, 122371. [CrossRef]
29. Saxena, P.; Shukla, P. Comprehensive review on fundamental properties and applications of poly (vinylidene fluoride)(PVDF). *Adv. Compos. Hybrid Mater.* **2021**, *4*, 8–26. [CrossRef]
30. Lu, H.; Li, J.; Guo, J.; Xu, Z. Movement behavior in electrostatic separation: Recycling of metal materials from waste printed circuit board. *J. Mater. Process. Technol.* **2008**, *197*, 101–108. [CrossRef]
31. Chu, H.N.; Kim, S.U.; Rahimian, S.K.; Siegel, J.B.; Monroe, C.W. Parameterization of prismatic lithium–iron–phosphate cells through a streamlined thermal/electrochemical model. *J. Power Sources* **2020**, *453*, 227787. [CrossRef]
32. Liu, Z.; Ma, H.; Fan, T.; Liu, M.; Zhao, Y. DEM investigation of the conveyor belt sorting system for coated fuel particles with a large feeding rate. *Powder Technol.* **2022**, *399*, 117160. [CrossRef]

Disclaimer/Publisher's Note: The statements, opinions and data contained in all publications are solely those of the individual author(s) and contributor(s) and not of MDPI and/or the editor(s). MDPI and/or the editor(s) disclaim responsibility for any injury to people or property resulting from any ideas, methods, instructions or products referred to in the content.